Batteries & Supercaps

Articles
doi.org/10.1002/batt.202100183

**Chemistry
Europe**
European Chemical
Societies Publishing

www.batteries-supercaps.org

Operando Terahertz Spectroscopy of Solid Electrolyte Interphase Evolution on Silicon Anodes

Daniel Krotkov+,[a, b] Dan Schneier+,[a] Svetlana Menkin,[c] Yonatan Horowitz,[a] Emanuel Peled,[a] Diana Golodnitsky,*[a, d] and Sharly Fleischer*[a, b]

The *in-situ* characterization of materials and interphases of battery electrodes is of crucial importance for the basic understanding of the complex, simultaneous processes that take place during the operation of secondary batteries. Here we present, for the first time, the use of a Terahertz (THz) time-domain-spectroscopy method for the *operando* characterization of the silicon/electrolyte interfacial phenomena and dynamics in a working lithium-ion battery. Strong correlation between the THz, XPS, and electrochemical data was established, allowing us to monitor the formation and evolution of the solid electrolyte interphase (SEI) during the reversible lithiation of the silicon anode.

1. Introduction

To understand the plethora of chemical reactions and associated phenomena taking place in electrochemical cells, researchers constantly strive to develop new *in-situ* and ultimately *operando*, non-detrimental characterization techniques. The activity of electrochemical cells leads to various ramifications, starting from unwanted chemical reactions among the different materials of the cell, through changes in structure and composition of the different components and materials. These result in large mechanical modifications that are generally destructive to the operation of the battery, severely degrade its performance and often compromise its safeness. In that respect, *operando*-characterization methods are highly desirable, as they offer on-line information about processes taking place in the electrochemical cell and provide the means to study these responses upon external stimuli, such as the applied voltage or current and their time duration.

Researchers of lithium-ion batteries have been searching for new and better characterization methods that could shed new light on various phenomena that invoke significant and often crucial hurdles to the many important applications. As the most prominent candidate for the next generation of anodes, silicon has become the subject of extensive research attempts that aim to utilize its high gravimetric capacity (roughly ten times that of current graphite anodes, normalized for the active material).[1] A major challenge in utilizing silicon for battery anodes emanates from its drastic volumetric changes during lithiation/delithiation,[2] which may lead to mechanical degradation of the electrode and the thick and unstable SEI formed on its surface.[3] The substitution of bulk silicon by nanometric particles of various shapes and structures aids to alleviate the issue of silicon pulverization,[4,5] although the stability of the whole electrode and the SEI are still a challenge and remain the subject of current research .[6,7] The study of the formation and evolution of the SEI typically encompasses electrochemical techniques combined with various spectroscopy approaches.[8–34] We have recently conducted in-depth electrochemical studies to mimic the lithium-ion-battery work-load profile and to study redox reactions associated with the evolution[3] and repair processes[35,36] of the SEI. However, some processes, such as the dissolution of the SEI products in the electrolyte (e.g., lithium ethylene dicarbonate, LiEDC), are practically undetected by electrochemical means, thus requiring non-detrimental, *operando* characterisation techniques.[37]

Here we present terahertz time-domain spectroscopy (THz-TDS) as a valid tool for monitoring the state of the SEI. THz-TDS is a well-established spectroscopic technique utilized in a variety of research fields.[38–41] As its name suggests, THz-TDS operates in the THz frequency range (10^{11}–10^{13} Hz) and provides the means for contact-free[37,42–44] and non-destructive dielectric characterization of complex systems under working conditions. In THz-TDS we analyze the frequency-resolved attenuation of the reflected/transmitted THz field, i.e., the complex electric field (amplitude and phase) following its interaction with a sample. The low THz photon energy ($\sim 10^3$

[a] D. Krotkov,+ D. Schneier,+ Dr. Y. Horowitz, Prof. E. Peled, Prof. D. Golodnitsky, Prof. S. Fleischer
School of Chemistry, Raymond and Beverly Sackler Faculty of Exact Sciences
Tel Aviv University
Tel Aviv-Yafo, 6997801 Tel Aviv, Israel
E-mail: golod@tauex.tau.ac.il
         sharlyf@tauex.tau.ac.il
[b] D. Krotkov,+ Prof. S. Fleischer
Tel-Aviv University Center for Light-Matter-Interaction
Tel Aviv 6997801, Israel
[c] Dr. S. Menkin
Department of Chemistry
University of Cambridge
Cambridge CB2 1EW, UK
[d] Prof. D. Golodnitsky
Wolfson Applied Materials Research Center
Tel Aviv University
Tel Aviv-Yafo, 6997801 Tel Aviv, Israel

[+] These authors contributed equally to this work.

Supporting information for this article is available on the WWW under https://doi.org/10.1002/batt.202100183

An invited contribution to a joint Special Collection between Batteries & Supercaps and Chemistry–Methods on In Situ and Operando Methods for Energy Storage and Conversion

lower than visible) and the relatively low peak intensity ($<$ 1 meV/cm) signifies THz-TDS as a non-destructive technique to probe the dielectric properties of matter. To accommodate THz-TDS in reflection configuration while conducting electrochemical tests we designed and manufactured an operational coin-cell battery equipped with a THz window. We followed and analyzed the evolution of the THz reflectivity throughout the electrochemical cycling of the Si/Li cell. Specifically, we studied the THz response to anodes consisting of silicon nanoparticles, a polymeric binder and a minor concentration of conductive carbon used to improve the efficiency of the lithiation process. While far from optimal in terms of battery performance, we chose this composition to provide both electrochemical activity (charge and discharge) and sufficient THz field penetration for *operando* characterization. In this work, we lay the groundwork for *operando* THz-TDS of the battery materials' interfaces by studying the THz reflectivity changes in correlation with well-established electrochemical-characterization methods. We further corroborate our *operando* THz analysis of the solid electrolyte interphase by Electrochemical Impedance Spectroscopy (EIS), and *ex-situ* depth-profile XPS. Our results reveal that the THz response stems from the formation and repair processes of the SEI following various degrees of damage induced by the charging voltage.

Experimental Section

Spectro-electrochemical coin cell

Metals act as mirrors in the THz range consequently precluding the penetration of the THz field through a typical casing of the coin cell or the current collector. Therefore, we designed our coin cell (Figure 1) to have minimal metallic components. Polyethylene terephthalate (PET) discs, 15 mm in diameter and 1 mm in thickness were used as both optical windows and anode substrate. To improve the adhesion of the silicon slurry to the PET, one side of the PET window was roughened by dripping acetone on its surface and wiping it off after 30 seconds. The anode composition was: lithiated polyacrylic acid (LiPAA, PAA $M_w = 450$ K was purchased from Sigma Aldrich and reacted with LiOH), sodium carboxymethyl cellulose (NaCMC, Sigma Aldrich), single-walled carbon nanotubes (SWCNTs, OCSiAl) and silicon nanoparticles (SiNPs, Tekna) at a ratio of [5:5:0.1:89.9]. The slurry was then applied on prepared discs and the anodes were dried under vacuum at 40 °C overnight before being transferred to an Argon-atmosphere glovebox (O_2 and $H_2O <$ 1 ppm, MBraun). The coin cells (model 2032, 20 mm diameter,
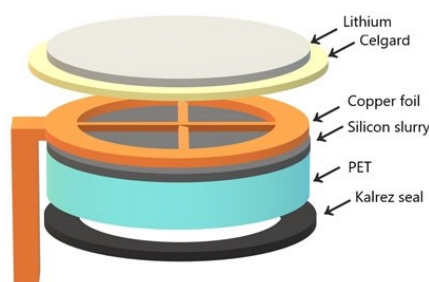
3.2 mm height) were assembled with the use of custom-made cell casings with a 12 mm hole drilled at their center. To seal the coin cell, a Kalrez ring (15/10 mm) was placed between the PET window and the coin-cell casing. To further reduce the metal content, copper foil (10 μm) was cut into "Q" shape and placed on top of the anode to maintain electrical connectivity. To ensure cycling at the center of the anode, two copper wires (130 μm) were placed across the anode's center. Metallic lithium was used for both the counter and reference electrodes, and was separated from the anode by a single Celgard 2400 separator. An electrolyte composed of 1 M $LiPF_6$ in EC:DEC (1:1) with 2% v/v VC and 15% v/v FEC (Solvay-Fluor). The cells were charged and discharged with the use of a PalmSens4 potentiostat (for charge/discharge profiles of conventional Si/Li cell see section SI.6 in the Supporting Information).

TDS-THz setup

The home-built THz-TDS spectrometer in reflection configuration,[42,45] is depicted in Figure 2(a). Briefly, a near-IR pulse (800 nm, 100 fs duration) from a chirped pulse amplifier (CPA) is split to form a strong near-IR pulse for THz generation (beam 1, Figure 2a) and a weak optical-readout pulse (beam 2, Figure 2a). The THz pulse is generated with the use of the tilted pulse front (TPF) optical rectification in a prism-cut $LiNbO_3$ crystal[46] and is routed through a 4-f reflection setup comprising two pairs of off-axis parabolic mirrors (OAPM), set at 15° and 90°. After the first pair of OAPMs, the incoming THz beam is focused on a ~ 10 mm spot size on the sample. The reflected THz beam is routed by the second pair of OAPMs to an electro-optic (EO) sampling module[47,48] for time-resolved detection of the THz field, $E_{THz}(t)$. In Figure 2(b), we present a typical single-cycle THz field generated in our setup, with a usable spectrum of 0.1–1.1 THz as shown in Figure 2(c). The THz field propagates in a humidity-free environment to avoid absorption by water vapor.[49]

2. Results and Discussion

2.1. Ex-situ THz-TDS

The custom-made coin cells consisted of a PET disc acting as both the transparent THz window and the substrate for the silicon electrode. We added a minimal amount of CNTs to the silicon anode slurry to increase its conductivity, since typically used additives such as graphite or acetylene black were found to be opaque to the THz field. The small amount of conductive material restricted the charge/discharge currents to 10–30 μA. The cell is placed at the sample position to reflect the impinging THz field (spot size of ~ 10 mm in diameter) to the EO sampling module. Figure 3 shows the *ex-situ* THz transient reflected from the PET window with and without the silicon electrode.

The PET-window surface was scanned twice: first, (blue curve in Figure 3) with the deposited anode sample and second, (red curve in Figure 3), after the anode material was rinsed away. THz transients corresponding to the THz reflection from the front, bare, side of the window (air-PET interface) are set as $t = 0$ ps and the back-side reflection (PET-anode interface) at $t \approx 12$ ps. This time delay is in a good agreement with the expected round-trip time of the THz field in the 1 mm PET

Figure 1. Scheme of the modified 2032 cell and assembly. The THz beam penetrates (reflects) the coin cell from bellow.

Labels in figure: Lithium, Celgard, Copper foil, Silicon slurry, PET, Kalrez seal
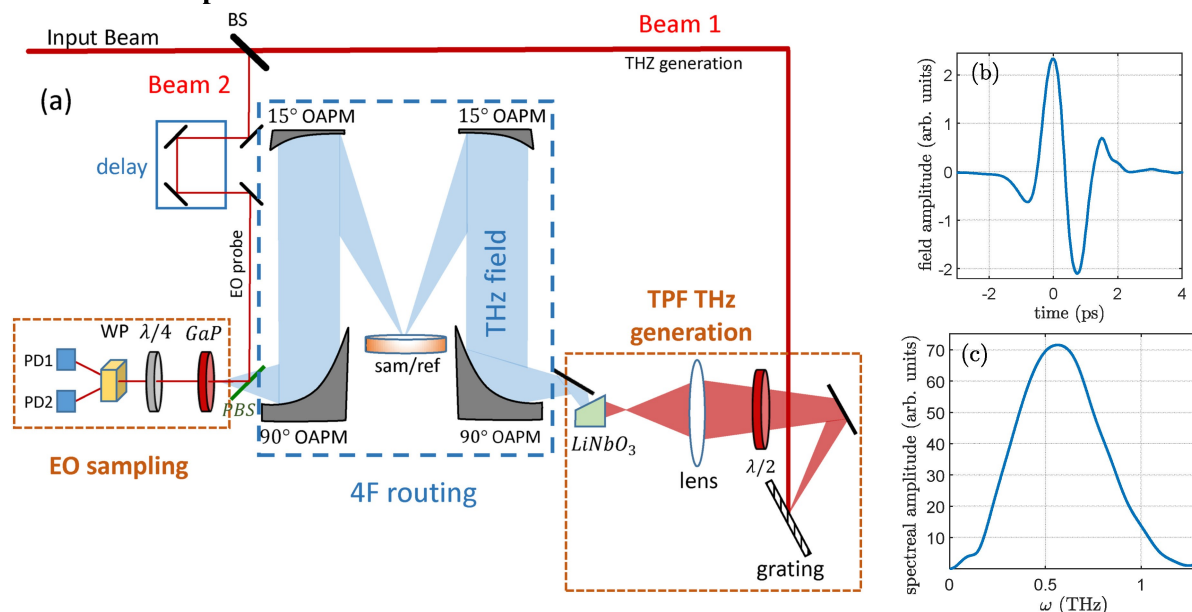
TDS-THz setup

Figure 2. a) Illustration of the time-domain THz spectrometer in reflection mode. The electrochemical cell was placed at the THz focal point (sam/ref. in the figure). A typical THz signal in the time domain is shown in b), with its spectral content in c). The EO sampling module includes a pellicle beam splitter (PBS), a Gallium Phosphate crystal (GaP), $\lambda/4$ waveplate, a wallaston prism (WP) and two photodiodes, PD1 and PD2.
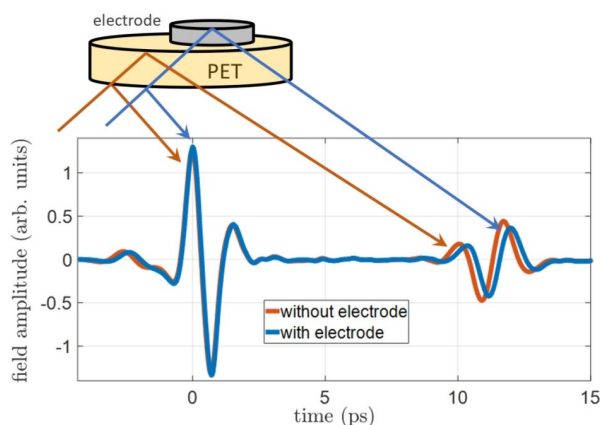

Figure 3. The THz signal of the PET substrate, with and without the presence of the silicon electrode (THz beam reflections depicted in blue and orange respectively). The THz transients are separated by 12 ps. The π-phase reversal is attributed to reflection from high to low refractive index, as predicted by the Fresnel equations. Note that only the signal reflected from the electrode (*back surface reflection*) changes with cycling conditions and holds the SEI information.

window. The round-trip time of the anode-covered PET is ~300 fs longer than that of the bare PET window, suggesting that the THz field propagates through the anode and reflects from the anode-air interface (rather than from the PET-anode interface) in this experiment, and the anode-electrolyte interface inside an operational cell. From the observed delay of ~300 fs in the silicon electrode we can estimate the thickness of the electrode to be ~25 μm for the electrode material (See Supporting Information Section SI.1). Thus, the results of Figure 3 indicate that the THz field propagates through the

electrode material and reflects from the backside of the electrode.

2.2. Operando THz Measurements

To monitor and follow the evolution of the electrode upon electrochemical activity within a working-battery cell, we performed multiple consecutive THz-TDS scans while cycling the cell. A single THz-TDS scan takes about 3–4 minutes to complete. The time-domain data and electrochemical profiles obtained at the same time are tagged with a mutual time stamp such that they can be presented on the same time axis. In Figure 4 we show two representative scans of the same cell (taken from the data of Figure SI2 in the Supporting Information); one under open-circuit conditions (blue curve), the other after prolonged cycling (purple curve).

The front-side and back-side (where the Si anode is placed) THz reflections are readily distinguished in the time-domain THz scans of Figure 4 since they are separated by ~12 ps. The front reflection (at $t = 0$, THz time) remains fairly unchanged throughout the cycling, whereas the THz reflection from the electrode (back-side at $t \sim 12$ ps) changes in both amplitude and phase, attributed to the electrochemical processes invoked by charge-discharge cycling. We note that laser instabilities during long operation may result in slight changes in the generated THz field amplitude, however, as evident from Figure 4 where both curves are normalized by the front reflection, the THz waveform remains unchanged.
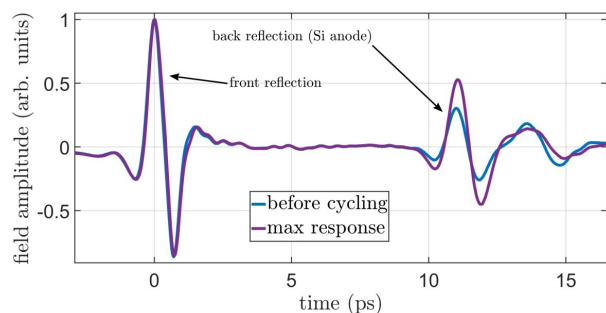
Figure 4. THz reflection from an operational coin cell. The blue curve depicts the initial state of the cell, as measured before the electrochemical process begins. As the process is underway, the electrode evolves and its signal (at $t \sim 12$ ps) is altered. The purple curve was measured ~ 8.3 hours into the process, when the signal exhibits its largest deviation from the initial state. Since laser instability can affect the measurement, the front reflection (at $t = 0$) is used as a reference relative to which the signals are normalized. These two THz scans were taken from the data presented in Figure SI2.

2.3. THz Data Analysis

Naturally, the dielectric properties of the air-PET interface remain unchanged throughout the cell operation since it does not participate in the electrochemical process. Therefore, the reflection from the front-side of the PET serves as a reference for the impinging THz field. We analyse the THz response in each scan as follows: we calculate the THz energy reflected from the front surface (P_{THz}^{front}) and from the back surface (P_{THz}^{back}) by integrating over the field intensity ($|E_{THz}|^2$) in the two corresponding time windows [Eq. (1)]:

$$P_{THz}^{front} = \int_{-4ps}^{4ps} |E_{THz}|^2 dt \ , \ P_{THz}^{back} = \int_{8ps}^{16ps} |E_{THz}|^2 dt, \qquad (1)$$

where the integration limits pertain to Figure 4. We calculate the THz signal for each scan as the ratio between the back (electrode) reflection and the front surface reflection, $THz_{signal} = P_{THz}^{back}/P_{THz}^{front}$, to account for possible laser-power instabilities that may take place during the several hours and often 1–2 days of continuous laser operation. We note that by integrating over the reflected THz intensity, our analysis is insensitive to the carrier-envelope phase variations observed in Figure 4 and thereby solely reveals the change in reflectivity. The THz_{signal} extracted from each scan is normalized with respect to the signal prior to the electrochemical cycling.

To verify that the changes in the THz transients are due to the SEI growth and evolution we used the impedance of the cell measured at the key stages of the cycling. In addition, at the end of each cycling protocol, we disassembled the coin cell and carried out depth-profile XPS scans.

2.4. Operando SEI Evolution

Figure 5 shows the experimental results obtained in a THz-TDS experiment performed during a single, 26 hour-long cycle (including rest, charge and discharge). Note that each THz data
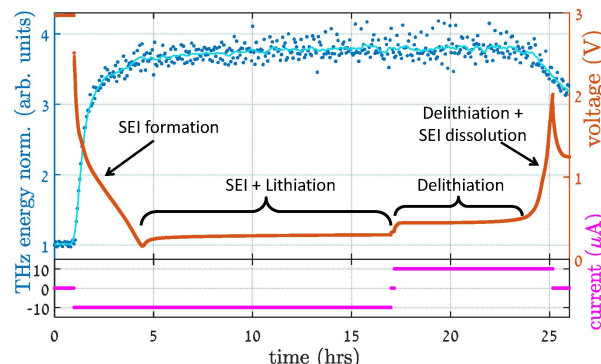

Figure 5. The THz signal (blue dots with a trendline in light blue) in the time domain measured over a single cycle; a discharge stage (1–17 hours) followed by a charge stage (18–26 hours). The cell voltage is shown in orange and the current in magenta.

point (blue points) corresponds to a 3–4 minute scan, while the voltage (orange) data points are collected with a time resolution of 10 seconds.

The first stage of the electrochemical procedure was a 45-minute rest stage (no applied potential or current), where the open-circuit voltage (OCV) of ~ 2.9 V was measured, as expected from a Si-anode vs. lithium cell.[50] During this rest stage, the THz signal is maintained at unity, thus guaranteeing that the forthcoming changes in the THz signal result from the electrochemical-cycling process. The rest stage was followed by a ~ 15 hours long discharge step at -10 μA during which the SEI is formed and the silicon electrode undergoes lithiation. Low discharge rate was chosen to allow the SEI to form in full. Next ($t = 16.5$ hours) we began to charge the battery at 10 μA (namely, inducing delithiation of the Si-anode). As most of the lithium has been removed from the anode, the voltage rises to the 2 V set limit (at $t = 24$ hours). Finally, we applied a rest stage (OCV) starting at $t = 25$ hours.

The results of Figure 5 unveil strong correlation between the THz signal and the state of the SEI layer: during the initial stage (1–5 hours) the dominant process is the SEI formation and the THz signal increases steeply to ~ 4 times its initial level. Thereafter, the THz signal reaches a plateau at 3.8 (i.e., $\times 3.8$ its initial level) while the SEI continues to evolve during the discharge of the electrode ($t = 5$–17 hours). During the charge step (17–25 hours) the THz signal remains constant as long as the SEI is still intact. Eventually, the depletion of residual lithium from the Si anode and SEI results in an abrupt rise in cell voltage to 2 V. This rise is accompanied by contraction of the electrode, which cracks and degrades the SEI,[3] and the partial dissolution of the SEI compounds that are stable only at low voltages,[37] overall indicating some deterioration of the SEI. Correspondingly, the THz signal decreases dramatically. The impressive sensitivity of THz-TDS to the dielectric properties of matter reveals itself at this point ($t > 25$ hours) as the THz signal continues to drop where no redox reactions take place and the cell potential dwindles to OCV. This stage is associated with the SEI deterioration due to continued dissolution of compounds that are unstable at high voltages. These trends were found consistent in several additional experiments described in detail

Batteries & Supercaps

Articles
doi.org/10.1002/batt.202100183

Chemistry
Europe
European Chemical
Societies Publishing

in the SI (Section SI1). The above findings suggest that the THz signal is primarily sensitive to the state of the SEI layer.

To further study the sensitivity of THz-TDS to minute changes in the SEI, we devised electrochemical protocols to avoid complete SEI formation and to distinguish this stage from the lithiation of the Si anode. In each cycling protocol, we induced three consecutive phases of rapid lithiation/delithiation cycles. The voltage during the three lithiation phases was limited to 0.8 V, 0.7 V and 0.6 V in order to avoid significant lithiation of the Si anode and ensure that the thickness of the Si anode is unaffected. Each lithiation stage is followed by a delithiation step limited to 2 V (THz-TDS results shown in Figure 7). In order to determine the SEI composition that this procedure will produce, we have conducted *ex-situ* XPS analysis on reference Si anodes casted on copper foil applied with comparable anode material loading and tested in a coin cell under the same conditions as the *in-situ* cells. We present in Figure 6(a) the *ex-situ* depth profile XPS of a Si-anode at its delithiated state following cycling according to the above protocol (2 V$\rightleftharpoons$0.8 V, 2 V$\rightleftharpoons$0.7 V, 2 V$\rightleftharpoons$0.6 V). The atomic concentration of silicon increases with the sputtering of the outer surface of the SEI ($t_{sputter} = 0$ minutes) to the Si bulk ($t_{sputter} = 6$ minutes) while the Li_{1s} and F_{1s} concentrations gradually diminish. The decrease of C1s, and O1s signals to a residual level can be attributed to the sputtering of the top SEI layer. Therefore, we deduce that after two minutes of sputter we have reached the bulk SEI, composed primarily of inorganic compounds. Another reference silicon anode was discharged once and held at 0.6 V for 60 hours, being delithiated only before the cell was disassembled. The depth profile of this sample is presented in Figure 6(b).
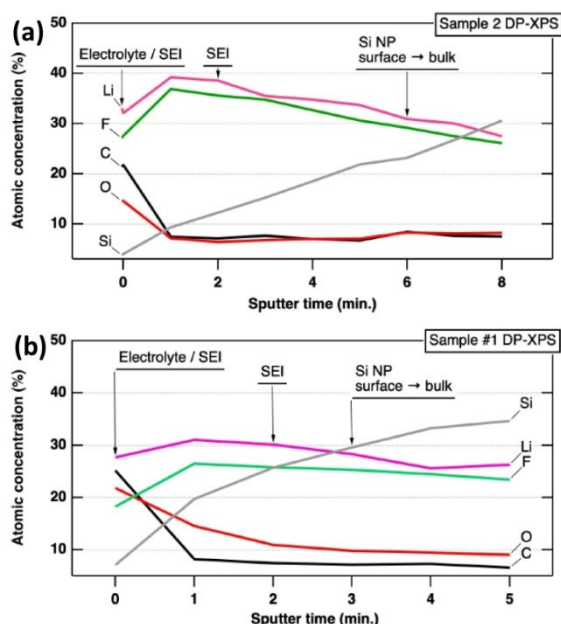
From our elemental analysis of the delithiated Si anodes we find that at these lithiation potentials a Li_xSiO_y phase forms together with an SEI.[9,51,52] The repetitive charge/discharge procedure of the sample in Figure 6(a) has led to an SEI with a higher content of inorganic species such as LiF and Li_2O than the sample in Figure 6b, but both show the clear characteristics of the mosaic structure of the SEI, combining inorganic and organic reduction products. High 2p resolution spectra of the samples are presented in section SI5 in the Supporting information. The Si 2p spectrum (Figure SI10) has the characteristics of cycled Si surfaces.[8] It exhibits an elemental Si asymmetric peak with the Si $2p_{3/2}$ and Si $2p_{1/2}$ overlapping together with a broad shoulder centered at ~102 eV, which we assign to Si–C (100.3 eV), Si–O (101.7 eV) and Li_xSiO_y (102.7 eV). The Li 1s, in Figure SI11, follows the expected SEI composition from a $LiPF_6$ and FEC electrolyte to show a prominent LiF peak (56.7 eV) and residual $LiCO_3$ (55.6 eV) and Li_2O (54.1 eV) peaks. The C1s spectrum (Figure SI12) has peaks at 286.5 eV and at ~290 eV, typical to species containing C–O and O–(C=O)–O, respectively. Overall, the two main conclusions to be drawn from this analysis are, that although incomplete, the SEI on silicon formed at 0.6 V can be considered "typical" SEI, and that repetitive delithiation induces changes in the structure of the SEI most likely as a result of partial dissolution of certain organic species at 2 V.

Figure 7 depicts the evolution of the THz signal throughout the abovementioned lithiation/delithiation protocol. In all of the short-duration cycles, we observe an increase in the THz signal upon SEI formation, followed by a fairly steady THz signal level during the rest period that follows each stage of SEI formation. Dramatic drop in THz signal is observed ONLY after the delithiation stage in each cycle is completed and the cell voltage rapidly increases to 2 V. We note that a closer look at the data reveals that in the first set (1–10.7 hours) the THz signal level seems to decrease also during the rest periods that follow each of the short SEI formation stages. In the second set
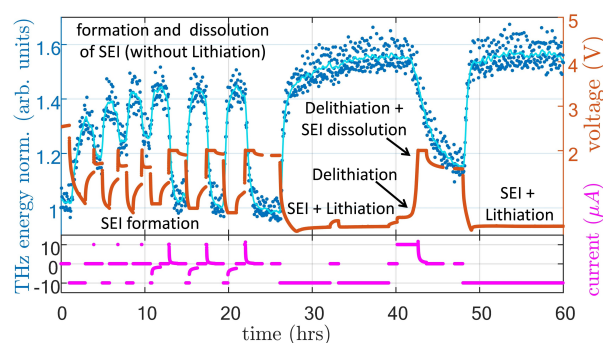

Figure 6. The depth profile of cycled cells obtained from the SEI after a) three consecutive lithiation stages limited to 0.8 V, 0.7 V and 0.6 V with delithiation stages ending at 2 V, b) a single discharge to 0.6 V with 60 hours at constant voltage before delithiation to 2 V.

Figure 7. The THz response to a process in several sequences. The experiment begins with 1 hour of rest, followed by three sets. **First set (1–10.7 hours):** lithiation - 1 hour rest - delithiation - 1 hour rest. This is repeated for different lower bounds of the lithiation voltage: 0.8 V, 0.7 V and 0.6 V. **Second set (10.7–24 hours):** lithiation to 0.8 V - 1 hour at 0.8 V–1 hour rest - delithiation to 2 V–1 hour at 2 V–1 hour rest and is repeated for 0.7 V and 0.6 V. This is followed by a longer rest of two hours (24–26 hours). **Third set (26–60 hours):** a regular lithiation-delithiation cycle (26–42.6 hours), followed by 1 hour of 2 V followed by ~4.5 hours rest, followed by another lithiation stage.

(10.7–24 hours) however, where the SEI is formed for longer periods (at the same voltages), the THz signal is better preserved during the rest stages after SEI formation and drops when the delithiation stage is completed as stated above.

The comparison between the two sets suggests that partially formed SEI (in the first set) is insufficiently stable and undergoes some changes that manifest by slow reduction in the THz signal. Evidence for such change can be found in electrochemical impedance spectroscopy (EIS) measurements, of the cell shown in Figure SI4. This cell was discharged to 0.6 V and held at 0.6 V for 48 hours, released to OCV for 7 hours and then held at 0.6 V for additional 12 hours. The EIS analysis, presented in Figure SI5 supports the effect that the rest step has on the resistance of the SEI. After the initial SEI formation, its resistance is roughly ~540 Ω. However, after 7 hours at rest it increases to above 900 Ω. A second step of constant voltage at 0.6 V lowers the resistance once again to ~540 Ω suggesting that the SEI formed at these potentials is not sufficiently stable to remain intact unless a discharge potential is applied. In addition, some organic SEI components may partially dissolve over prolonged rest, which makes the SEI more porous, virtually thicker and resistant. The same cell was then cycled for several short SEI-forming cycles and a longer lithiation/delithiation cycle. The corresponding THz signal is presented in Figure SI.4 of the Supporting Information.

To verify that the THz-TDS indeed probes the surface (SEI) and is less affected by the near-surface silicon phase (Si→Li_xSi)[53] we induced a long lithiation period, i.e., constant current without voltage limitation for 12 hours (starting at $t=$ 26 hours with a 1 hour rest at 33–34 hours in Figure 7). A more prominent example of our conclusion is provided by the third set. Here the rest stage follows a long lithiation and SEI formation stage that provides fully formed SEI (rather than partially formed SEI as in the first set). Indeed, the THz signal remains constant during rest and demonstrates significant reduction only when the delithiation stage is completed and the cell voltage jumps to 2 V (at 42.6 hours) at which it is held for 1 hour and then left at OCV for 4.5 h.

It is rather well established that formation of the initial SEI on silicon occurs typically during the first lithiation. The kinetics of the redox reactions may be very fast, depending on the type of electrolyte and additives, thus resulting in stable and compact SEI. However, as found by several researchers including our previous works,[3,17,35,36] the SEI on Si undergoes partial changes in its morphology and thickness upon cycling. This is caused by continuing expansion/contraction of the anode upon lithiation/delitiation. The reactions of the "newly released silicon surface" with the electrolyte are more pronounced for the anodes containing very low concentration of lithium in the silicon particles and at the silicon/electrolyte interface. With neutron reflectometry,[17] it was found that the thickness of the SEI layer increases to about 250 Å on delithiation and decreases to 180 Å with increasing Li content (Li3.7Si) in the silicon anode. As can be seen in Figure 7, the strong change in the THz signal is detected in anodes which undergo short-term partial lithiation/delithiation (high-voltage cut-off) cycles. However, the THz signal vs. time curve is gently inclined on prolonged lithiation/delithiation. These observations are in a good correlation with the previous reports.[3,17,35,36]

While some as yet unknown chemical reactions, or mechanical degradation of the SEI may occur, we suggest that this is the dissolution of LiEDC and other organic species in the electrolyte,[54] which starts at the completion of delithiation and continues during the rest stage. Here, as is evident by the THz-TDS, we notice that prolonged delithiation stages at high voltages (~2 V) result in the degradation of the SEI, albeit due to its enhanced dissolution following silicon anode delithiation, rather than parasitic redox reactions, since the current drops to (nearly) zero.

Nonetheless, when compared to the decrease in THz signal observed in the second set of rapid cycling, we find that the THz level reached, after forced delithiation and a 5-hour rest period, levels of the value of ~1.2, suggesting that the prolonged SEI formation results in an SEI that may not be fully stable but still sufficiently substantial to be detected.

3. Conclusions

Our results show that THz-TDS can detect alterations of the elusive SEI layer under cycling conditions, and more importantly, during rest periods. By on-line monitoring of the THz reflectivity from the electrode-electrolyte interface within a working electrochemical cell, we were able to identify the SEI formation on the surface of the Si electrode during the lithiation process, and its partial dissolution during prolonged delithiation. Our measurements show that certain parts of the SEI tend to dissolve during rest periods if not fully formed before, demonstrating the importance of efficient complete SEI formation in batteries. The presented technique lays the basis for utilizing terahertz spectroscopy as a uniquely desirable tool in the ever-growing field of *operando* characterization of electrochemical cells.

Conflict of Interest

The authors declare no conflict of interest.

Batteries & Supercaps

Articles
doi.org/10.1002/batt.202100183

Chemistry Europe
European Chemical
Societies Publishing

[1] W.-J. Zhang, *J. Power Sources* **2011**, *196*, 13–24.
[2] L. Y. Beaulieu, K. W. Eberman, R. L. Turner, L. J. Krause, J. R. Dahn, *Electrochem. Solid-State Lett.* **2001**, *4*, A137.
[3] E. Peled, S. Menkin, *J. Electrochem. Soc.* **2017**, *164*, A1703–A1719.
[4] D. Schneier, Y. Shaham, K. Goldshtein, M. Goor, D. Golodnitsky, E. Peled, *J. Electrochem. Soc.* **2019**, *166*, A740–A746.
[5] X. H. Liu, L. Zhong, S. Huang, S. X. Mao, T. Zhu, J. Y. Huang, *ACS Nano* **2012**, *6*, 1522–1531.
[6] Y. Jin, S. Li, A. Kushima, X. Zheng, Y. Sun, J. Xie, J. Sun, W. Xue, G. Zhou, J. Wu, F. Shi, R. Zhang, Z. Zhu, K. So, Y. Cui, J. Li, *Energy Environ. Sci.* **2017**, *10*, 580–592.
[7] T. Jaumann, J. Balach, T. Jaumann, J. Balach, U. Langklotz, V. Sauchuk, M. Fritsch, A. Michaelis, V. Teltevskij, D. Mikhailova, S. Oswald, M. Klose, G. Stephani, R. Hauser, J. Eckert, L. Giebeler, *Energy Storage Mater.* **2017**, *6*, 26–35.
[8] M. Nie, D. P. Abraham, Y. Chen, A. Bose, B. L. Lucht, *J. Phys. Chem. C* **2013**, *117*, 13403–13412.
[9] B. Philippe, R. Dedryvèere, M. Gorgoi, H. Rensmo, D. Gonbeau, K. Edström, *Chem. Mater.* **2013**, *25*, 394–404.
[10] B. Philippe, R. Dedryvèire, M. Gorgoi, H. Rensmo, D. Gonbeau, K. Edström, *J. Am. Chem. Soc.* **2013**, *135*, 9829–9842.
[11] C. Xu, F. Lindgren, B. Philippe, M. Gorgoi, F. Björefors, K. Edström, T. Gustafsson, *Chem. Mater.* **2015**, *27*, 2591–2599.
[12] G. G. Eshetu, T. Diemant, S. Grugeon, R. J. Behm, S. Laruelle, M. Armand, S. Passerini, *ACS Appl. Mater. Interfaces* **2016**, *8*, 16087–16100.
[13] S. M. Bak, Z. Shadike, R. Lin, X. Yu, X. Q. Yang, *NPG Asia Mater.* **2018**, *10*, 563–580.
[14] K. P. C. Yao, J. S. Okasinski, K. Kalaga, I. A. Shkrob, D. P. Abraham, *Energy Environ. Sci.* **2019**, *12*, 656–665.
[15] C. Cao, H. G. Steinrück, B. Shyam, K. H. Stone, M. F. Toney, *Nano Lett.* **2016**, *16*, 7394–7401.
[16] H. G. Steinrück, C. Cao, Y. Tsao, C. J. Takacs, O. Konovalov, J. Vatamanu, O. Borodin, M. F. Toney, *Energy Environ. Sci.* **2018**, *11*, 594–602.
[17] G. M. Veith, M. Doucet, J. K. Baldwin, R. L. Sacci, T. M. Fears, Y. Wang, J. F. Browning, *J. Phys. Chem. C* **2015**, *119*, 20339–20349.
[18] J. Yang, A. Kraytsberg, Y. Ein-Eli, *J. Power Sources* **2015**, *282*, 294–298.
[19] A. Krause, O. Tkacheva, A. Omar, U. Langklotz, L. Giebeler, F. Fauth, T. Mikolajick, W. M. Weber, *J. Electrochem. Soc.* **2019**, *166*, A5378–A5385.
[20] D. Alves Dalla Corte, G. Caillon, C. Jordy, J.-N. Chazalviel, M. Rosso, F. Ozanam, *Adv. Energy Mater.* **2016**, *6*, 1501768.
[21] L. Yu, H. Liu, Y. Wang, N. Kuwata, M. Osawa, J. Kawamura, S. Ye, *Angew. Chem. Int. Ed. Engl.* **2013**, *52*, 5753–5756.
[22] W. T. Liu, Y. R. Shen, *Proc. Natl. Acad. Sci. USA* **2014**, *111*, 1293–1297.
[23] Y. Horowitz, H.-L. Han, P. N. Ross, G. A. Somorjai, *J. Am. Chem. Soc.* **2016**, *138*, 726–729.
[24] N. G. Rey, D. D. Dlott, *J. Electroanal. Chem.* **2017**, *800*, 114–125.
[25] E. Talaie, P. Bonnick, X. Sun, Q. Pang, X. Liang, L. F. Nazar, *Chem. Mater.* **2017**, *29*, 90–105.
[26] U. Westerhoff, K. Kurbach, F. Lienesch, M. Kurrat, *Energy Technol.* **2016**, *4*, 1620–1630.
[27] Y. Horowitz, H.-G. H.-G. H.-G. Steinrück, H.-L. H.-L. H.-L. Han, C. Cao, I. I. I. I. Abate, Y. Tsao, M. F. M. F. Toney, G. A. G. A. Somorjai, *Nano Lett.* **2018**, *18*, 2105–2111.
[28] Y. Horowitz, H.-L. Han, F. A. Soto, W. T. Ralston, P. B. Balbuena, G. A. Somorjai, *Nano Lett.* **2018**, acs.nanolett.7b04688.
[29] Y. Horowitz, I. Ben-Barak, D. Schneier, M. Goor-Dar, J. Kasnatscheew, P. Meister, M. Grünebaum, H.-D. Wiemhöfer, M. Winter, D. Golodnitsky, E.

[continued] Peled, *Batteries & Supercaps* **2019**, *2*, 213–222; Supercaps **2019**, 2, 213–222.
[30] G. G. Eshetu, T. Diemant, S. Grugeon, R. J. Behm, S. Laruelle, M. Armand, S. Passerini, *ACS Appl. Mater. Interfaces* **2016**, *8*, 16087–16100.
[31] Y. Wang, V. Yu, X. Guo, E. Peled, S. Greenbaum, *Journal of Power Sources*, **2001**, *94*, 230–237.
[32] A. L. Michan, G. Divitini, A. J. Pell, M. Leskes, C. Ducati, C. P. Grey, *J. Am. Chem. Soc.* **2016**, *138*, 7918–7931.
[33] C. Cao, B. Shyam, J. Wang, M. F. Toney, H.-G. Steinrück, *Acc. Chem. Res.* **2019**, *52*, 2673–2683.
[34] J. Li, J. R. Dahn, *J. Electrochem. Soc.* **2007**, *154*, A156–A161.
[35] T. Mukra, E. Peled, *J. Electrochem. Soc.* **2020**, *167*, 100520.
[36] E. Peled, D. Schneier, Y. Shaham, G. Ardel, L. Burstein, Y. Kamir, *J. Electrochem. Soc.* **2019**, *166*, A2091.
[37] I. Hasa, A. M. Haregewoin, L. Zhang, W.-Y. Tsai, J. Guo, G. M. Veith, P. N. Ross, R. Kostecki, *ACS Appl. Mater. Interfaces* **2020**, *12*, 36 acsami.0c09384.
[38] H. Y. Hwang, S. Fleischer, N. C. Brandt, B. G. Perkins, M. Liu, K. Fan, A. Sternbach, X. Zhang, R. D. Averitt, K. A. Nelson, *J. Mod. Opt.* **2015**, *62*, 1447–1479.
[39] S. Zhong, *Front. Mech. Eng.* **2019**, *14*, 273–281.
[40] T. Kampfrath, K. Tanaka, K. A. Nelson, *Nat. Photonics* **2013**, *7*, 680–690.
[41] T. Kiwa, Y. Akiwa, H. Fujita, T. Teranishi, K. Sakai, H. Nose, M. Kobayashi, K. Tsukada, *J. Infrared, Millimeter, Terahertz Waves* **2020**, *41*, 430–437.
[42] M. E. Layani-Tzadka, D. Krotkov, E. Tirosh, G. Markovich, S. Fleischer, *Nanotechnology* **2019**, *30*, 215702.
[43] Y.-J. Tsai, C.-Y. Chang, Y.-C. Lai, P.-C. Yu, H. Ahn, *ACS Appl. Mater. Interfaces* **2014**, *6*, 630–635.
[44] C. T. Nemes, J. R. Swierk, C. A. Schmuttenmaer, *Anal. Chem.* **2018**, *90*, 4389–4396.
[45] D. Krotkov, E. Flaxer, S. Fleischer, *OSA Continuum.* **2020**, *3*, 3365.
[46] J. Hebling, K. Yeh, M. C. Hoffmann, B. Bartal, K. A. Nelson, *J. Opt. Soc. Am. B* **2008**, *25*, B6.
[47] A. Nahata, A. S. Weling, T. F. Heinz, *Appl. Phys. Lett.* **1996**, *69*, 2321–2323.
[48] Q. Wu, X.-C. Zhang, *Appl. Phys. Lett.* **1995**, *67*, 3523–3525.
[49] Y. Yang, A. Shutler, D. Grischkowsky, *Optics Express* **2011**, *19*, 8830–8838.
[50] D. Schneier, Y. Shaham, G. Ardel, L. Burstein, Y. Kamir, E. Peled, *J. Electrochem. Soc.* **2019**, *166*, A4020–A4024.
[51] E. Radvanyi, W. Porcher, E. De Vito, A. Montani, S. Franger, S. Jouanneau Si Larbi, *Phys. Chem. Chem. Phys.* **2014**, *16*, 17142–17153.
[52] E. Radvanyi, E. De Vito, W. Porcher, S. Jouanneau Si Larbi, *J. Anal. At. Spectrom.* **2014**, *29*, 1120–1131.
[53] K. Ogata, E. Salager, C. J. Kerr, A. E. Fraser, C. Ducati, A. J. Morris, S. Hofmann, C. P. Grey, *Nat. Commun.* **2014**, *5*, 1–11.
[54] N. Saqib, C. M. Ganim, A. E. Shelton, J. M. Porter, *J. Electrochem. Soc.* **2018**, *165*, A4051.